Title: **Assessment of Damage Containment Features of a Full-Scale PRSEUS Fuselage Panel through Test and Teardown**

Authors: Andrew C. Bergan
John G. Bakuckas Jr
Andrew E. Lovejoy
Dawn C. Jegley
Jonathan Awerbuch
Tein-Min Tan

ABSTRACT

An area that shows promise in enhancing structural integrity of aircraft and aerospace structures is the integrally stitched composite technology. The most recent generation of this technology is the Pultruded Rod Stitched Efficient Unitized Structure (PRSEUS) concept developed by Boeing Research and Technology and the National Aeronautics and Space Administration. A joint test program on the assessment of damage containment capabilities of the PRSEUS concept for curved fuselage structures was conducted recently at the Federal Aviation Administration William J. Hughes Technical Center. The panel was subjected to axial tension, internal pressure, and combined axial tension and internal pressure load conditions up to fracture, with a through-the-thickness, two-bay notch severing the central stiffener. For the purpose of future progressive failure analysis development and verification, extensive post failure nondestructive and teardown inspections were conducted. Detailed inspections were performed directly ahead of the notch tip where stable damage progression was observed. These examinations showed: 1) extensive delaminations developed ahead of the notch tip, 2) the extent and location of damage, 3) the typical damage mechanisms observed in composites, and 4) the role of stitching and warp-knitting in the failure mechanisms. The objective of this paper is to provide a summary of results from these posttest inspections.

Andrew C. Bergan, FAA-Drexel Fellowship Student, FAA William J. Hughes Technical Center, Atlantic City International Airport, NJ 08405, U.S.A.
John G. Bakuckas, Jr. FAA William J. Hughes Technical Center, Atlantic City International Airport, NJ 08405, U.S.A.
Andrew E. Lovejoy and Dawn C. Jegley, NASA Langley Research Center, Hampton, VA 23681, U.S.A.
Jonathan Awerbuch and Tein-Min Tan, Department of Mechanical Engineering and Mechanics, Drexel University, Philadelphia, PA 19104, U.S.A.

INTRODUCTION

A primary goal of stitched composites technology is to provide improved through-thickness mechanical properties for composite laminates and structures [1]. Early studies focused on using stitches to suppress delamination damage [2]. Subsequent studies of stitched composite technology showed that introducing fibers in the through-the-thickness direction could substantially improve fracture toughness [3-5] and damage tolerance [6-8]. As stitching provided a promising alternative to costly toughened matrices or interleafing concepts, it was chosen as a key area in the National Aeronautics and Space Administration (NASA) Advanced Composite Technology (ACT) program [9], which aimed to gain the increased benefit of the weight savings and performance potential offered by composite primary structures. Composite structures utilizing bonded or co-cured joints experience similar deficiencies resulting from the relatively weak matrix interface. Therefore, in applications that must sustain significant out-of-plane loading such as primary aircraft structure, mechanical fasteners have often been used. Selective stitching provides an alternative to mechanical fasteners by stitching the stiffeners to the skin [10]. Element tests of blade stiffened specimens where the stiffener flange-skin interface was reinforced with through-the-thickness stitching showed a significant increase in failure load in compression after impact tests [11, 12].

The latest generation of integrally stitched composite, the pultruded rod stitched efficient unitized structure (PRSEUS) concept [13], shows promise as an alternative to conventional composite structure technology for application to primary aircraft structure [14-21]. A key feature of the PRSEUS concept is through-the-thickness stitching, which suppresses out-of-plane damage and creates a damage-arresting behavior, nearly eliminating the need for mechanical fasteners. This advantage over conventional composite structures allows it to operate at higher strain levels, directly translating into weight savings for structure sized by damage tolerance and residual strength requirements. The damage arrestment capability of the PRSEUS concept was first demonstrated through a flat panel test [14]. Additional subcomponent-level tests of damage arrestment in: 1) minimum-gauge axial tension test panel, 2) out-of-plane loading of a minimum-gauge panel, and 3) buckling of a large span were conducted to further validate the PRSEUS concept [15, 16]. A pressure cube was tested to investigate the assembly joints required for application of the PRSEUS concept to large structures [17].

In the current program, NASA, the Federal Aviation Administration (FAA), and Boeing Research and Technology (Boeing) have partnered in an effort to assess the damage-containment features of a full-scale curved PRSEUS panel. The purpose of this joint program was to: 1) demonstrate that a curved PRSEUS panel meets the strength and damage tolerance requirements described in Title 14 Code of Federal Regulations (CFR) Part 25 [22] and 2) characterize the damage progression of a curved PRSEUS panel. The PRSEUS fuselage panel was designed and fabricated by Boeing and NASA and tested using the FAA Full-Scale Aircraft Structural Test Evaluation and Research (FASTER) facility [23]. A description of the design and fabrication process and an overview of the test results, which showed that the test panel met the first goal, have been summarized in [24-26].

This paper focuses on the second goal by providing a description of the damage progression of the panel with a two-bay notch and subsequent posttest

nondestructive and destructive investigation of damage ahead of a notch tip. Detailed inspections were performed directly ahead of the notch tip where stable damage progression was observed. Results from this study will be used in future efforts to develop and verify progressive failure analyses.

CURVED TEST PANEL CONFIGURATION AND MATERIAL

The PRSEUS fuselage panel used dry warp-knit carbon fabric materials stitched together and co-cured with a vacuum assisted resin transfer molding (VARTM) process [13]. The warp-knit fabric stack consists of 0°, 90°, and ±45° plies held together by through-the-thickness knitting. The panel was 3,226 mm long, 1,905 mm wide, and had a 2,286-mm radius, as shown in Figure 1(a). The panel consisted of a skin and substructure which were stitched together using a one-sided stitching process. The substructure consisted of seven full-length rod-stiffened stringers and five foam-core frames. The cross sections of the frame and stringer are shown in Figure 1(b) and (c), respectively. The red dashed arrows indicate the locations of the stitch rows that attached the stiffener flanges to the skin. The stringer consisted of a web with a unidirectional pultruded carbon fiber rod at the top which provided an uninterrupted load path. The test section of the panel represented a section of an aircraft fuselage. The test section skin consisted one stack with a layup of $[-45/+45/90_2/0/90_2/+45/-45]$, which results in a skin thickness of approximately 1.3 mm. The area surrounding the test section included additional build-up plies for load introduction. Further details of the design, materials, lay-up, and fabrication of the test panel are available in [24].

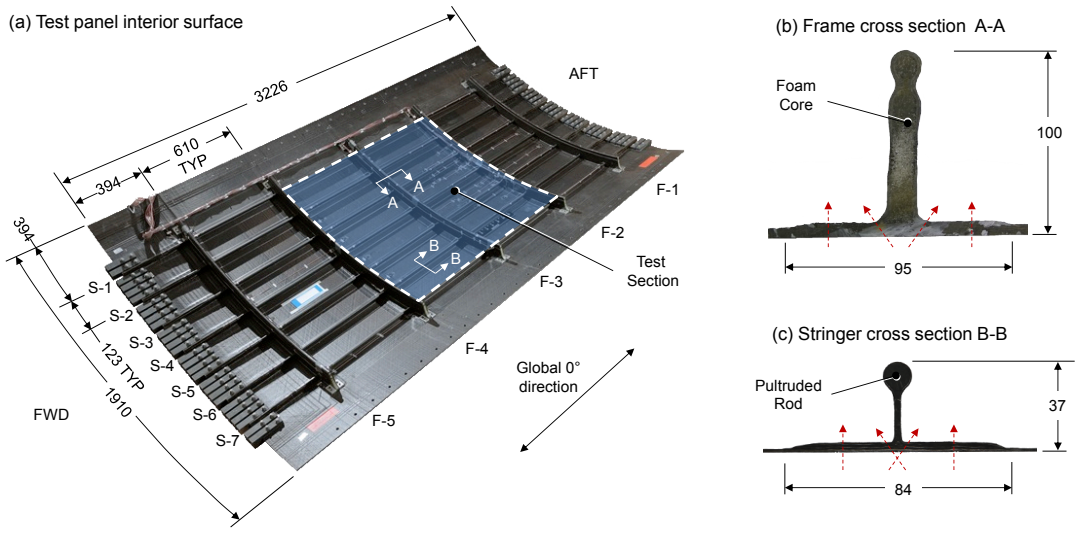

Figure 1. Photographs of the PRSEUS test panel. All dimensions are in mm.

EXPERIMENTAL PROCEDURE

The panel was tested using the FASTER test fixture at the FAA William J, Hughes Technical Center. Details of the test fixture and the modifications made for this test are provided in [23] and [25], respectively.

Test Phases

The test program included three test phases:

- Phase I: the pristine panel loaded to limit load levels to provide baseline data and to show compliance with the limit strength requirements of 14 CFR 25.305;
- Phase II: the panel with barely visible impact damage (BVID) was loaded to ultimate load levels to show compliance with the ultimate strength requirements of 14 CFR 25.305;
- Phase III: the panel with a through-the-thickness, two-bay notch severing the central stiffener, was loaded to limit loads to show compliance with 14 CFR 25.571, and then to monitor the failure process while increasing axial load until catastrophic fracture occurred.

This paper focuses on Phase III results and posttest investigations. Key results for Phase I and Phase II are described in [26]. Pressure loads were based on an operating pressure of 63.4 kPa, designated as 1.0 P, and the axial loads were based on a design limit load (DLL) of 1010 kN. The loading goal of Phase III was for the panel to sustain: 1) 1.15 P pressure only load, 2) 1.0 P and 100% DLL combined load, and 3) 100% DLL axial only load.

In Phase III, notch tip damage growth was monitored throughout loading up to the panel's catastrophic fracture. The 200 mm, two-bay notch, was cut through the BVID to minimize any effect of the BVID on Phase III testing, as shown in Figure 2. Loading was applied in a series of loading steps (LS), in increasing severity, from pressure only to axial only, as the most likely sequence to achieve all loadings determined from the pretest analysis [24]. The five LS are as follows:

LS-1: Pressurization to 1.15 P;
LS-2: Maintain pressure at 1.0 P and increase the axial load to 100% DLL;
LS-3: Unloading pressure while maintaining the axial load at 100% DLL;
LS-4: Pressurization to 1.0P while maintaining the axial load at 100% DLL;
LS-5: Maintain pressure at 1.0 P while increasing the axial load to catastrophic fracture.

Loading was applied in a single experiment and all target loads were reached while never completely unloading the panel, thus, ensuring that no additional damage occurred during unloading as a result of crack closure (e.g., local fiber buckling). Internal pressure loads were reacted by minimal axial loads, which were based on a closed pressure vessel assumption.

Deformation and state of damage were monitored throughout the three phases of the test program using conventional strain gages, LVDTs, digital image correlation and interior and exterior cameras [26]. In addition, acoustic emission (AE) data was recorded during the test to provide an additional record of damage formation and progression. The AE results are presented in [27].

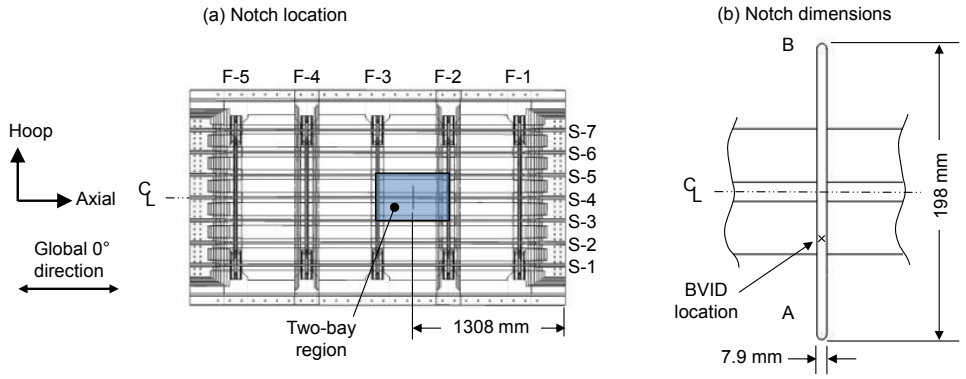

Figure 2. The two-bay notch.

Posttest Inspection Methods

After fracture, the panel was inspected with a variety of NDI methods and then a teardown evaluation using visual and fractographic examinations. The details of the procedures used for all posttest inspections are described in the following section.

NONDESTRUCTIVE INSPECTION

Pulse-echo ultrasonic, flash thermography, and x-radiography computed tomography (CT) scans were taken after catastrophic fracture in the vicinity of the notch tip B (only half the panel was available for posttest inspection). The regions scanned are shown in Figure 3 for each method used. Visual inspection was performed throughout the interior and exterior surface of the panel. Details of the three advanced NDI methods used are described as follows:

- Pulse-echo ultrasound: A Mobile Automated Ultrasonic Scan (MAUS V) system was used to identify the nonvisible damage region boundaries. The pulse-echo inspection provided amplitude and time-of-flight results. The pulse-echo scan was performed at 5 MHz using a 6.35-mm diameter, delay-line probe, which is a common choice for composite based on typical flaw size. The MAUS V system was programmed to increment 0.15 mm in the axial direction after each pass.
- Flash Thermography: A Raytheon Radiance HSX camera with Mosaiq software was used to compare the ultrasonic and flash thermography NDI results. The camera sensitivity was 0.025°C. Six images were taken of the damaged region from the notch tip to the outer stringer (S-6).
- X-Radiographic CT: A Kimtron 450 set to 200kV and 3.5mA, which created a poly energetic isotropic x-ray beam and a Perkin Elmer XRD1620 detector, was used to identify the approximate locations of delaminations in the thickness direction. The specimen size was limited because of the detector size, thus a 200- by 450- mm specimen was machined from the panel, which consisted of the notch tip and first adjacent stringer (S-5). The resolution was 0.15 mm per voxel.

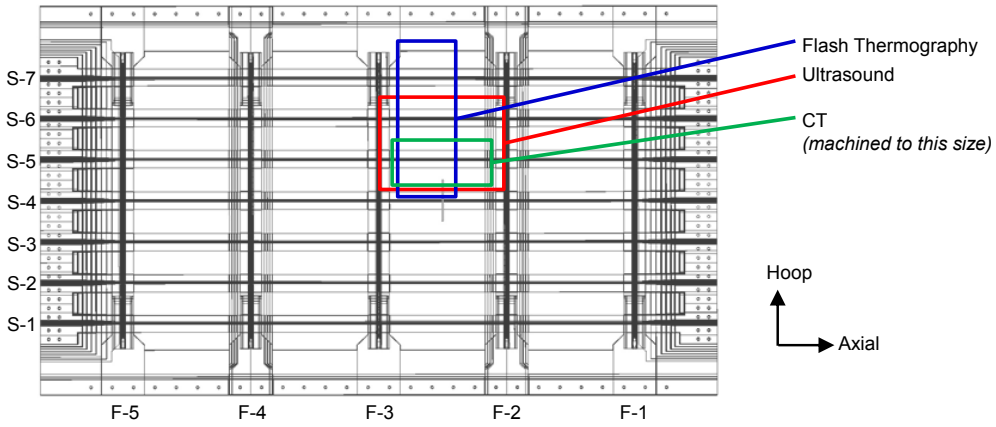

Figure 3. Areas inspected with each NDI method

A carbide cutting wheel with a conventional grinder and an oscillating cutting tool was used to remove the CT specimen from the panel. During this process, the specimen was reinforced around the perimeter, including attachment of the stringer to the skin, to limit vibration and potential damage inflicted during machining. A similar cutting procedure was used for the destructive inspection, which is described in the following section.

DESTRUCTIVE INSPECTION

The region of the panel directly ahead of notch tip B, which was machined out of the panel for CT inspection was examined visually in a teardown evaluation to determine the extent and location of damage. Failure in each ply was assessed qualitatively using visual inspection aided by low magnification light microscopy for the purpose of future comparisons with progressive failure analyses. Additionally, selected segments cut from this region, as shown highlighted in Figure 4, were examined using a scanning electron microscope (SEM) to determine the failure mechanisms active.

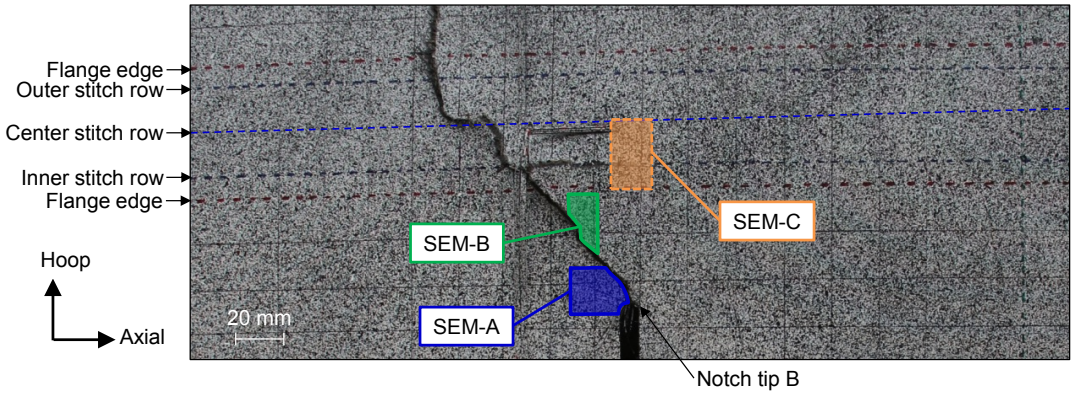

Figure 4. Locations of posttest inspections.

Three key areas were examined in the fractography study: 1) the damage formation region at the notch tip, denoted SEM-A, 2) the delaminated surface ahead of the notch tip, denoted SEM-B, and 3) the disbonded surface on the stringer flange of the skin/stringer interface including the stitch failure of the first stringer ahead of the notch, denoted SEM-C. All SEM specimens were less than 40 mm in length and width to fit within the SEM chamber.

The three specimens inspected were excised from regions of stable damage growth, as observed prior to catastrophic failure, where the effects of the dynamic catastrophic failure are assumed to be minimal because strain measurements indicated that this region was almost completely unloaded before fracture. The fractography examinations were performed using a Phillips/FEI XL30 environmental SEM. The specimens were sputter coated with a conductive layer of Platinum and Palladium with a thickness of approximately 10 nm.

RESULTS AND DISCUSSION

The key results recorded during Phase III, which showed the notch tip damage initiation, progression, arrest, and final panel fracture and the posttest NDI and teardown, are presented in this section.

The five-step loading sequence load history, applied in Phase III, is shown in Figure 5. Also shown in Figure 5 are key damage progression observation points, denoted with capital letters A-H. Note that during the final load step, the hydraulic pump of the loading fixture briefly shut down, resulting in a short duration of constant axial load, which upon resumption was followed by a brief higher axial loading rate, as shown in Figure 5(b) just before label ‘E’.

Visual Observations of Damage Formation and Progression

Stable damage progression was observed visually, on the exterior and interior starting during LS-2 and intermittently thereafter until catastrophic fracture occurred. Major damage progression occurred during LS-2 and LS-5, thus the following discussion focuses on these load steps. Recall that the pressure was maintained constant at 1.0 P while the axial load increased monotonically in LS-2 and LS-5, therefore, only the axial load level will be stated in the foregoing discussion.

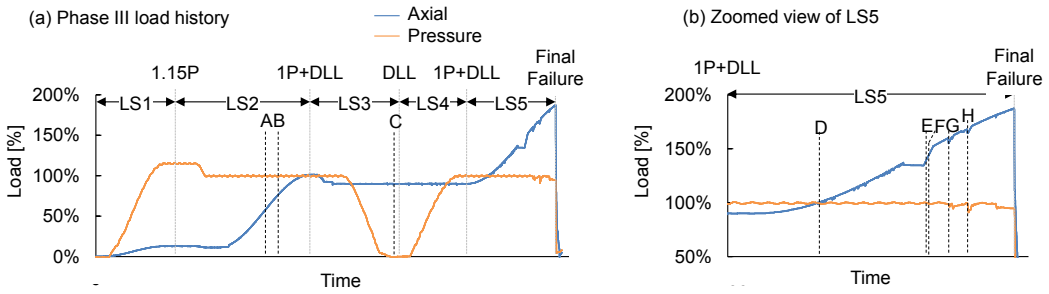

Figure 5. Phase III load history with key damage progression observations letter A-H.

INTERIOR SURFACE

Photographs of the crack progression on the interior are shown in Figure 6. Visible damage formation was first observed at 58% DLL (point A in Figure 5) in the form of a matrix crack on the interior surface, propagating antisymmetrically from the two notch tips, as shown in Figure 6(a). Subsequent damage accumulation ahead of both notch tips was intermittent in the form of several 45° matrix cracks, which propagated to the adjacent stringer flange edges as axial load was increased, as shown in Figure 6(b) to (e).

At the load level of 140% DLL, point E in Figure 5, extensive skin/stringer disbonding progressed through the entire width of the bay, evidenced by visible cracks along the skin/stringer interface, as partially shown in Figure 6(f). The skin/stringer disbonds were arrested by the stitching in the frame flanges as load was increased, and remained completely contained between the frames F-2 and F-3 by the stitching up to fracture. A large number of matrix cracks were observed along the 45° inner surface ply, emanating from the notch tips and stringer flanges. Visible damage on the interior surface was widespread as compared with the single crack progression seen on the exterior surface, described in the following section.

EXTERIOR SURFACE

Damage was observed visually on the exterior surface of the panel in a form of a crack along the 45° fibers of the outer ply, at 70% DLL (point B in Figure 5), as shown in Figure 7(a). Throughout the remainder of LS-2, damage progressed along the 45° direction, parallel to the outer ply fibers, in the form of a single matrix crack, as shown in Figure 7(a) to (c). Figure 7(c) shows the extent of damage at the end of LS-2, where the visible crack had extended 33 mm from the notch tip.

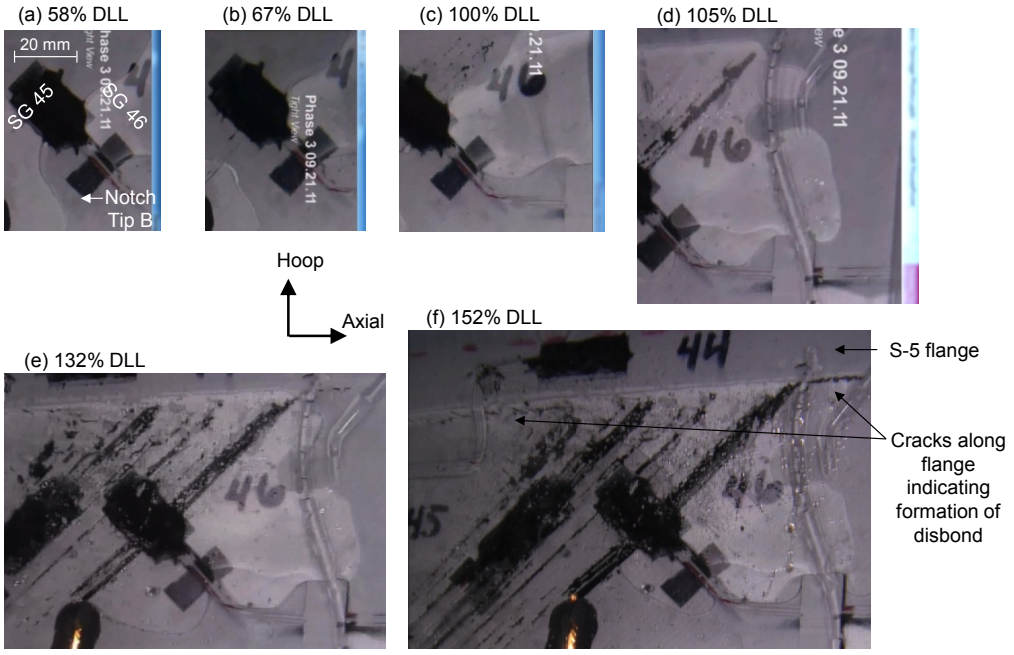

Figure 6. Photographs of notch tip A interior surface damage showing crack progression.

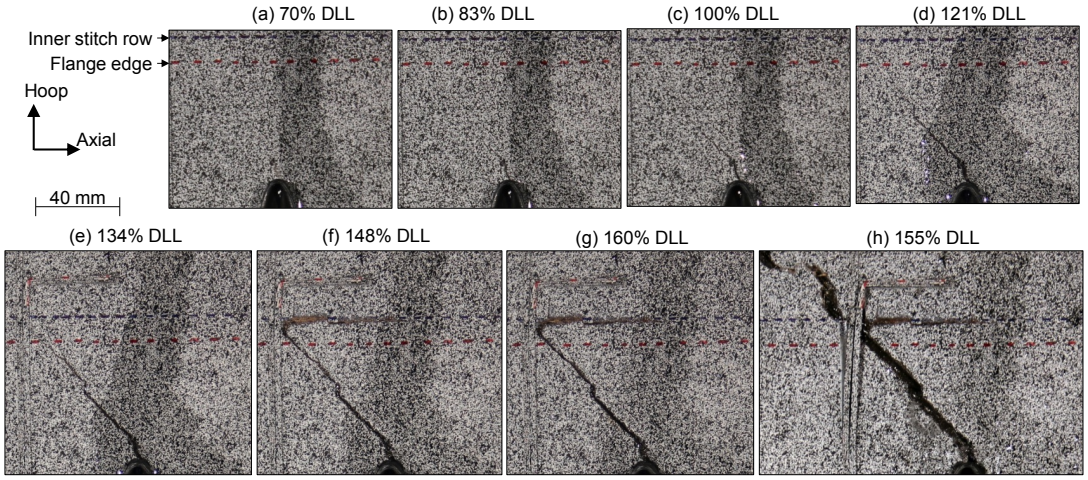

Figure 7. Photographs of notch tip B exterior surface damage showing crack progression.

As the axial load was increased above 100% DLL up to 147% DLL, notch tip crack progression was slow, stable, intermittent, and along the 45° direction and was then arrested by the inner row of stitches, as shown in Figure 7(d) and (e). When the load was further increased to 148% DLL, the crack at notch tip progressed instantaneously from the edge of the stringer flange to the inner stitch row (point F in Figure 5), before being arrested the second time, as shown in Figure 7(f), apparently due to load redistribution.

Additional axial load was required to progress the crack beyond the stringer. When the load reached 160% DLL, the damage progressed instantaneously beyond the two-bay region (point G in Figure 5) and out of the field of view of the exterior camera, as shown in Figure 7(g) and (h). The energy stored in the panel was released by the sudden formation of extensive damage, including the extension of the crack beyond stringer S-2, which caused a 5% axial load drop (from 160% DLL in Figure 7(g) to 155% DLL shortly afterward in Figure 7(h)). High speed video footage showed that damage progressed beyond the stringer nearly instantaneously (less than 0.2 ms). Similar crack progression was observed along the other notch-tip in terms of the extent, rate, and the intermittent nature of crack progression. A nearly identical crack initiation and progression pattern was observed along the other notch-tip.

MEASUREMENTS OF DAMAGE LENGTH

Exterior damage lengths were measured for load up to 160% DLL (point G in Figure 5) where damage propagated beyond the two-bay region. Interior damage lengths were measured up to the point where damage reached the adjacent stringers, S-3 and S-5 (point E in Figure 5). The exterior and interior crack length measurements are shown in Figure 8. The interior crack length was consistently slightly greater than the exterior crack length. The results clearly indicate a nearly constant crack growth rate up to 148% DLL. At that load level, a large damage extension is seen which corresponds to the instantaneous damage growth event where damage progressed along the stitch row.

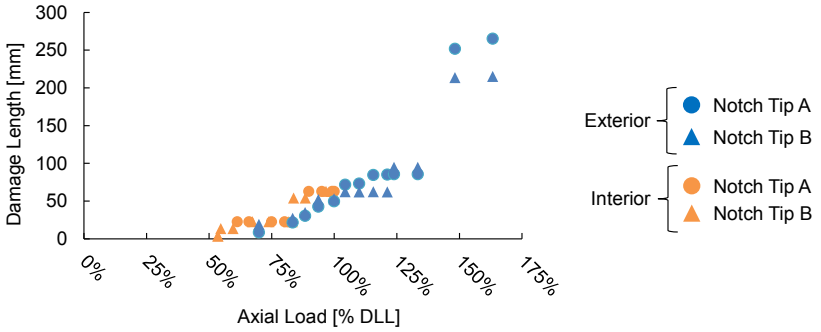

Figure 8. Crack progression up to point G in Figure 5 showing constant crack growth rate during LS-2 and LS-5.

At 160% DLL damage progressed outside of the two-bay region and the camera's field of view, thus no further damage length measurement was possible.

Load, Strain, and Displacement Redistribution

Damage progression was evident through strain records, which showed several strain redistributions occurred before fracture load was reached. The axial strains recorded by selected strain gages are shown in Figure 9 for monotonic axial loading in LS-1, LS-2, and LS-5. The locations of the strain gages are shown in the schematics of Figure 9(a) and Figure 9(b). Figure 9(a) also shows the state-of-damage ahead of the notch tip at the load of 140% DLL (point E in Figure 5). The correlation between strain redistributions and key visual observations of damage progression (i.e. points A through H shown in Figure 5), is shown by overlaying points A through H on the strain plots in Figure 9.

In LS-2, strain gages mounted in the two-bay region indicated damage progression, while those mounted outside the two-bay region indicated no affect from damage progression as seen in Figure 9(c) from 60% to 100% DLL. That is, while damage propagated through the two-bay skin, damage remained contained within the two-bay region.

During LS-5, significant strain redistribution was observed at 160% DLL, when damage progressed beyond the two-bay region. The four strain gages on the interior skin near the mid-bay, SG 37, SG 38, SG 39, and SG 40, shown in Figure 9(c), showed a sudden reduction in the local strain, indicating failure of the skin.

Note that SG 37 and SG 40 are equidistant from the panel edges and measure almost the same strains. This behavior indicates that the load introduction was uniform through a load of 160% DLL. Strain gages SG 38 and SG 39, which were located in the same bays as the notch tips, exhibited several discontinuities throughout loading from 100% to 160% DLL, corresponding again to the intermittent nature of damage accumulation. The massive damage accumulation observed in the skin at 160% - 165% DLL, as shown post-failure in Figure 10, nearly completely unloaded the skin in these four bays. The strains in the stringers S-6, S-5, S-3, and S-2 (recorded by SG 41, SG 43, SG 51, and SG 53, respectively) are nearly identical, as show in Figure 9(d), and show a sudden increase in strain at 160% DLL.

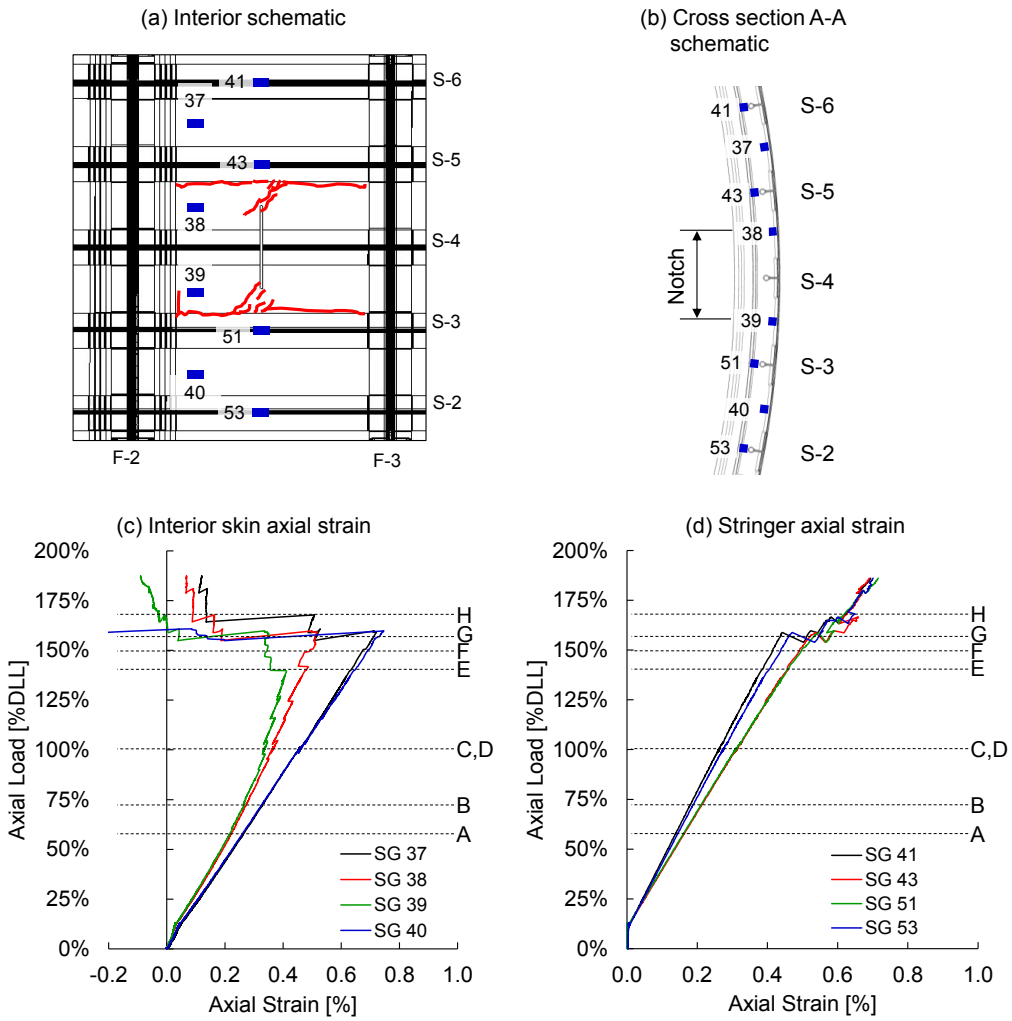

Figure 9. Strain results during monotonic axial of LS-1, LS-2, and LS-5.

That is, the stitched stringers bridged the failed skin (despite the local skin/stringer disbonding), and carried most of the load up to fracture. The results also show the symmetry of the strain distribution as manifested by the strain records of stringers S-2 and S-6 (SG 53 and SG 41, respectively) and stringers S-3 and S-5 (SG 51 and SG 43, respectively) throughout the failure process.

Posttest Inspections

Detailed post failure nondestructive and destructive inspections were conducted to determine the extent of damage and identify the dominant failure process and mechanisms. Results are presented for visual observations, ultrasound, flash thermography, CT inspections, and fractography. Note that the load level at which damage occurred, including whether damage occurred in the quasi-static loading or in the dynamic event of failure, cannot be determined from posttest examinations, however, identifying the damage mechanisms can be used to evaluate design and analysis methodologies.

NON-DESTRUCTIVE INSPECTIONS (NDI)

Visual

Visible damage was found to be significantly more widespread on the interior than the exterior faces. Figure 10 shows a side-by-side comparison of exterior and interior surface photographs.

The exterior crack was contained between frames F-2 and F-3 whereas the interior damage extended throughout the interior of the panel. The outer surface crack path turned at several stitching rows. The interior surface damage includes numerous matrix cracks, all oriented along the 45° direction, apparently emanating from the progressing through-the-thickness crack and stringer flanges, in an anti-symmetric manner.

No evidence of failed stitches was detected during loading by the interior or exterior cameras; however numerous stitches appear to have failed during the dynamic events of the catastrophic fracture. Posttest, complete disbonding between the stringers and the skin was observed in all stringers except S-4. Typical disbonds are shown in Figure 11(a) and Figure 11(b). The disbonding was accompanied by additional matrix cracking along the 45° direction as portions of the interior skin were delaminated, as shown in Figure 11(a). Such disbonding also occurred between the frame and the skin, as seen in the intersection between stringer S-7 and frame F-2 in Figure 11(b).

Additionally, no evidence of damage to the frame-stringer intersection or the stringer itself was observed prior to catastrophic fracture. However, severe damage, such as shown in Figure 11(c), was evident in the posttest evaluation. It should be noted that the cameras recorded panel motion at failure, when a large and sudden release of energy was manifested in a dynamic damage event. The failures shown in Figure 11 could have occurred at maximum load or during the subsequent dynamic event.

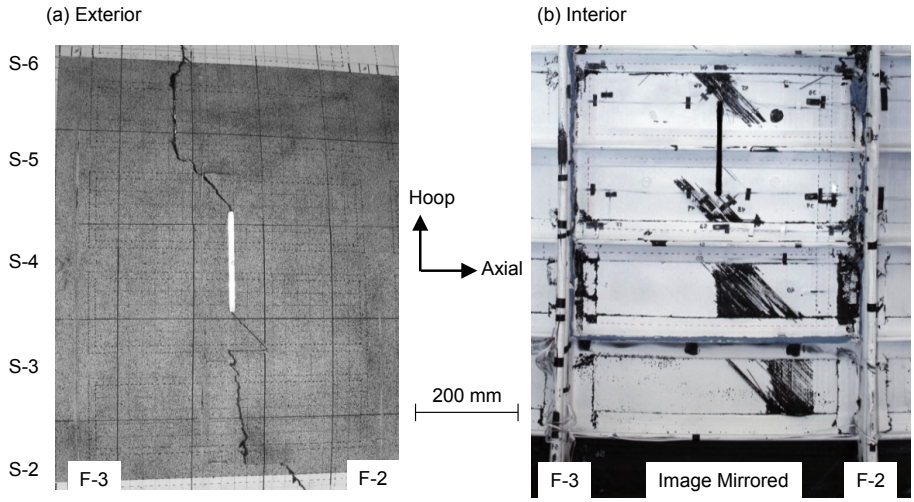

Figure 10. Post failure photographs of the panel.

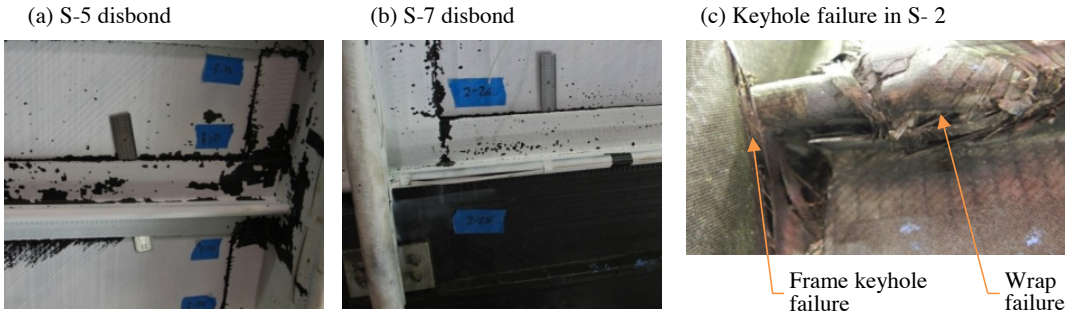

Figure 11. Post fracture photographs of several stringers and frames.

Ultrasound

The pulse-echo ultrasonic inspection encompassed an area that measured 610 mm x 406 mm, which included frames F-2 to F-3 in the axial direction and from notch tip B to stringer S-6 in the hoop direction. Amplitude and time-of-flight results clearly indicate a large delaminated region in the skin ahead of the notch tip, as shown in Figure 12. The reduction in amplitude and increase in time-of-flight in the frame areas indicate the frames are still partially attached to the skin, Figure 12(a) and Figure 12(b), whereas the stringers are completely disbonded. The time-of-flight near F-2 is longer than near F-3 because the structure was thicker near F-3 due to a skin splice joint. The time-of-flight C-Scan, shown in Figure 12(b), indicates that the nearest delamination to the outer surface, which surrounds the crack path, occurred at approximately the same location through-the-thickness throughout the inspected region. Due to limitations of this inspection, conclusions regarding the number of delaminations through-the-thickness could not be drawn. Some of the 45° matrix cracking around the crack path is visible in both the amplitude and time-of-flight results.

Flash Thermography

Flash thermography inspection showed very similar results as seen from the pulse-echo ultrasonic C-Scan. However, the 45° cracks on the interior surface were less clearly shown in the flash thermography results.

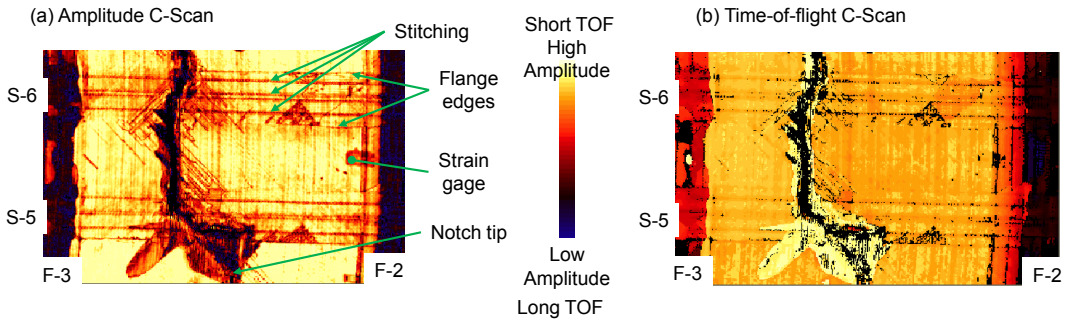

Figure 12. Pulse-echo C-Scans of the notch tip B region showing significant delamination at the notch tip and partial frame/stringer disbonding.

Based on the results from this test, both flash thermography and pulse-echo ultrasound produced suitable results for identifying the approximate extent and location of damage, however pulse-echo ultrasound is preferred for more detailed results with similar time to setup and scan.

X-Radiographic CT

The x-radiographic CT provided insight into the skin delaminations and the skin/stringer disbonding. Similar delamination size was identified as seen in the ultrasonic results. Multiple delaminations through the thickness were clear in the CT results. No stitching was visible along the skin/stringer disbonded area, which confirmed that the stitches completely failed at this interface. In the surrounding portions of the stringer, the stitching was intact on the exterior surface of the skin and interior surface of the stringer flange. Section view through the skin/stringer interface showed some areas with holes (i.e. voids) in the skin where the stitches apparently pulled-out, which indicated that the stitch failure occurred somewhere in the skin, rather than at the skin/stringer interface.

DESTRUCTIVE INSPECTIONS

Teardown examinations of key segments of the panel were performed to quantify the extent and location of damage, and to identify areas for subsequent fractography in order to identify the failure mechanisms.

Global Observations

Visual inspections of teardown of stringer S-5 confirmed that it was not attached to the skin. Figure 13(a) and Figure 13(b) show the skin and stringer segments and the disbond surfaces. In the photo shown in Figure 13(b), the stringer was lifted off the skin and rotated 180° about the hoop axis. The disbond surface revealed the mostly intact warp-knitting and broken stitches, as shown in Figure 13(c) and Figure 13(d).

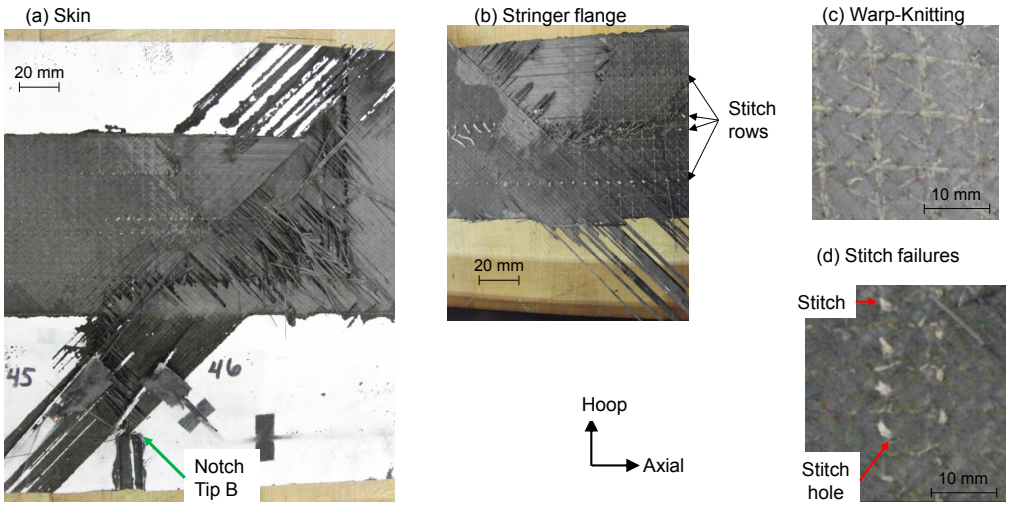

Figure 13. Visual inspection of tear down segments of the S-5 skin stringer disbond

The failed stitches appeared similar on both the skin and stringer disbond surfaces with small segments of the stitch protruding approximately 0.5 mm from each surface, indicating that the stitches mostly failed at the skin/stringer interface and that the stitches stretched. In some instances, particularly along the translaminar damage path, a much longer segment of the stitch (up to several millimeters) was observed protruding from the laminate, indicating the stitch failure occurred somewhere other than the skin/stringer interface. In two regions delamination of the skin and stringer flange occurred such that the failure between the skin and stringer did not occur uniformly at the skin/stringer interface. In these areas, the warp-knitting failed, in addition to the stitches.

Ply-by-Ply Teardown

Teardown of the skin showed delaminations, extensive matrix cracking in nearly all plies, and a well-defined crack path in all but the 90° plies. A schematic representation of the major crack path and delaminations are shown in Figure 14 for each ply through-the-thickness from the exterior ply shown in Figure 14(a) to the interior ply shown in Figure 14 (g). The exterior ply (-45°) shows the damage that was visible on the exterior surface, as shown in Figure 14(a). A crack extends in the -45° direction, parallel to the ply fiber direction, from the notch tip to the inner stitch row. The crack branched at this point, and the secondary crack progressed along the stitch row approximately 80 mm before terminating. The main crack progressed along the stitch row in the opposite direction briefly, and then continued in the hoop direction. The next ply (+45°) shows a slightly different crack path, as shown in Figure 14(b). The crack progressed in the hoop direction to the inner stitch row, and then continued along the same path as seen on the exterior ply.

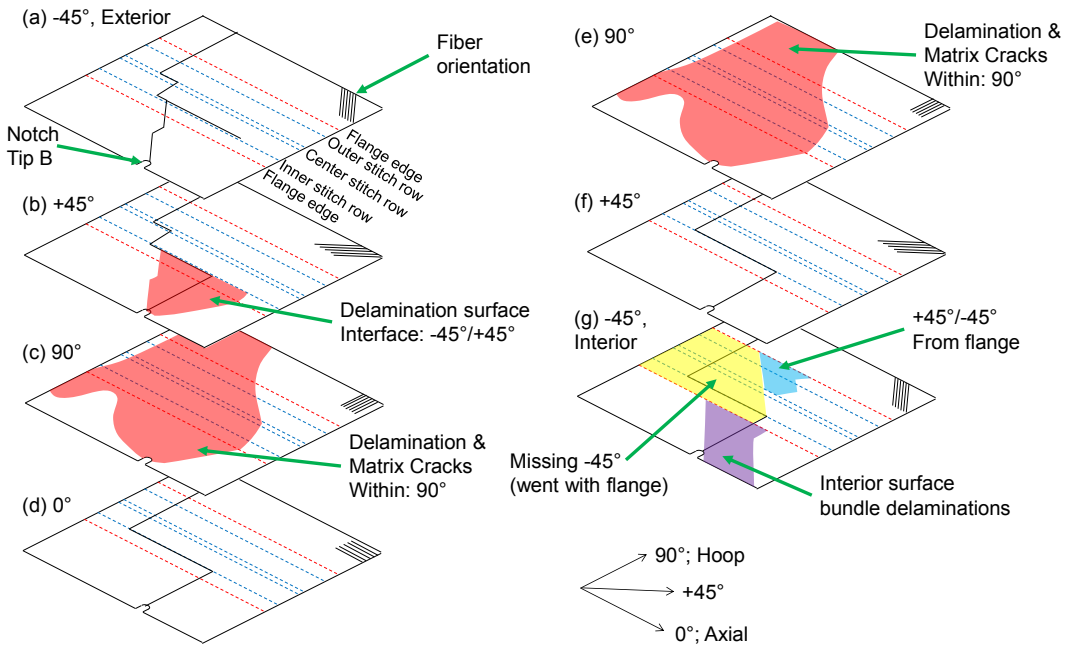

Figure 14. Schematic of significant failure extent, ply-by-ply.

A delamination was seen between the +45° and -45° ply, bounded by the inner stitch row and the 45° crack in the outer ply, as shown highlighted in red in Figure 14(b). The third ply (90°, double thickness) showed extensive delamination within the ply, as shown by the large region highlighted in red in Figure 14(c). In the select areas which were destructively examined, this delamination matched the delamination size and shaped detected by the ultrasonic inspection. The fourth ply (0°, center ply in layup) showed a crack in a similar location as the second ply with slightly different path between the inner stitch row and the outer stitch row, as shown in Figure 14(d). The fifth ply (90°) showed very similar damage as the third ply, which had the same orientation. The sixth ply (+45°) showed the same crack path seen in the central ply (0°) and no delaminations. The last ply, (-45°, interior surface) showed the same crack path as the central and sixth plies. In the region highlighted in blue in Figure 14(g), delamination in the stringer flange left the +45° and -45° plies from the flange on the skin. The yellow highlight region shows where the -45° ply from the skin delaminated and stayed with the stringer flange. Extensive delaminated bundles occurred between the notch and the flange, as shown highlighted in blue. This ply-by-ply damage map will be used for comparisons with damage predicted by future progressive failure analysis.

Fractography

Fracture surface morphology in the notch tip region and in the stringer/skin interface is described in this section. The fracture surface across the skin thickness (segment SEM-A in Figure 4), along the crack emanating from the notch tip, shows typical failure modes in graphite/epoxy laminates, including matrix cracking, delamination, and fiber breakage, as shown in Figure 15(a). Most of the adjacent plies at the notch tip have delaminated. A representative close-up view indicates that most fibers fractured perpendicular to their axis with no fiber pullout, Figure 15(b). Fiber surfaces in the 0° and 45°-plies were clean of matrix residue, with scattered matrix debris remaining on the fiber surface, as shown in Figure 15(b), indicating a complete fiber/matrix interface disbonding and relatively weak fiber/matrix interface.

The ultrasonic inspections revealed a relatively wide delaminated area ahead of the notch tip (see Figure 12). Examination of this delamination surface (segment SEM-B in Figure 4) revealed resin-rich areas around the warp knitting, as shown in Figure 16(a). The warp knitting process disturbs the path of the fibers causing the fibers to bend around the knitting, resulting in resin rich pockets and non-uniform fiber distribution and orientation. The width of the resin rich area is the width of the warp-knit thread, which is approximately 400 μm. The length was observed to be 6 to 8 mm. Figure 16(b) shows a detail view of a representative warp-knit failure region showing interface failure between the matrix and knitting fibers as well as knitting fiber pull-out and cleavage type fracture surfaces, characteristic of brittle fracture, in the resin-rich pocket surrounding the knitting. Previous studies [28] indicated warp-knitting may reduce the in-plane properties. Results from this investigation show that warp-knitting did affect the failure mechanism, and therefore may be important to the failure process. Close examination of the delaminated fracture surface also reveals that the fiber surface is clean of matrix indicating weak fiber/matrix bonding and matrix serrations characteristic of shear failure, as shown in Figure 16(c).

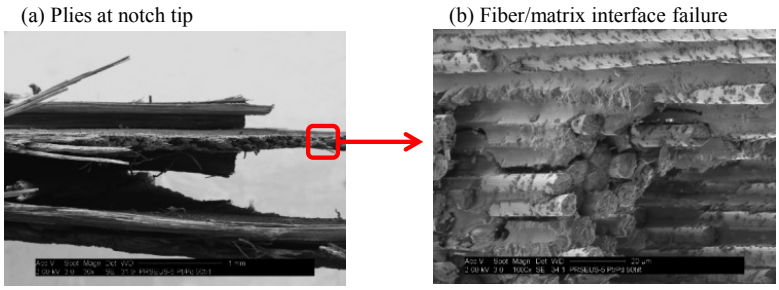

Figure 15. Fracture surface morphology across the skin thickness and along a crack emanating from the notch tip, segment SEM-A (see Figure 4).

Figure 16. Fracture surface of a delaminated region ahead of the notch tip, segment SEM-B (see Figure 4).

The skin stringer disbond area (segment SEM-C in Figure 4) exhibited regularly spaced matrix serrations, apparently as a result of shear failure, as shown in Figure 17(a) and Figure 17(b). Fiber imprints on the disbond surface indicate failure at the fiber/matrix interface. The surface was generally covered with matrix debris and some areas showed fiber bundles, Figure 17(c). A typical broken stitch, from the inner stitch row of stringer S-5 closest to the notch tip on specimen SEM-C, is shown in Figure 18(a). As seen, the stitch failed in tension, as a result of the skin/stringer disbonding, with its end spreading-out in a broom-like failure. The stringer flange and the skin apparently came in contact during the dynamic fracture process, pressing and crushing the end of the stitch. No indication of stitch/matrix interfacial disbonding was observed.

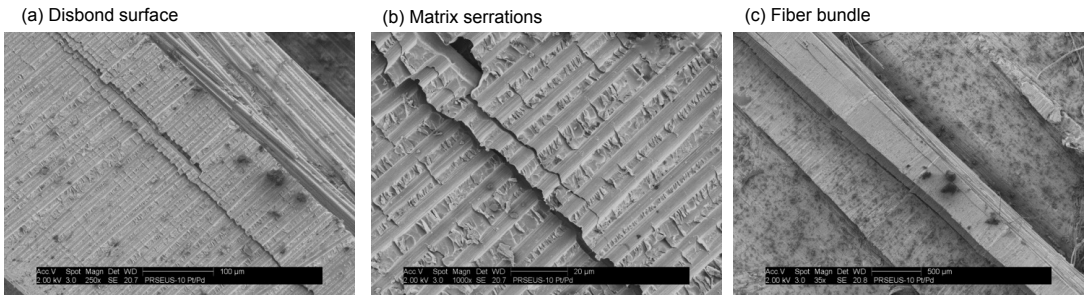

Figure 17. Fracture surface morphology of the resin-rich disbond region ahead of the notch tip, segment SEM-C (see Figure 4).

Figure 18. Characteristic failures of stitches located in the first stitched row of S-5, immediately ahead of the notch tip, segment SEM-C (see Figure 4).

However, because stitch stretching was noted, it is likely there was some degree of stitch/matrix interfacial disbonding; further investigation is required to examine this interface. As mentioned previously, in some areas, the stitches failed inside the laminate, resulting in a hole on the flange surface. One example is shown in Figure 18(b) with a tilted detail view of holes surface shown in Figure 18(c). Imprints and portions of the stitch thread remained on the resin-rich surface.

The SEM results revealed weak fiber/matrix interface bonding in the regions examined which provides a plausible explanation for the multiple widespread delaminations ahead of the notch tip. Additionally matrix serrations indicate a Mode II dominant failure [29] in the delaminated and disbonded regions. These results show the active failure mechanisms that should be considered and provide a basis for development and verification of future tensile progressive failure analysis of PRSEUS.

SUMMARY

In summary, a PRSEUS fuselage panel was subjected to different combinations of internal pressure and axial tensile loading to show compliance with the strength and damage tolerance requirements of 14 CFR 25. The final phase of testing included characterization of damage progression while loading to catastrophic failure with a two-bay, through-the-thickness notch severing the central stringer and adjacent skin. The successful test showed compliance with the strength and damage tolerance requirements of 14 CFR 25. Visual observations of damage progression on the interior and exterior were correlated with strain redistributions.

Posttest visual inspections revealed that the damage on the interior was much more extensive compared with the single, meandering crack observed on the exterior. The interior damage included extensive delamination ahead of the notch tips, skin/stiffener disbonding and stitch failure, and extensive matrix cracking along the surface ply fiber-direction. The dynamic event of the fracture caused disbonding of the frames and generally widespread stitch failure. The specific size and shape of the post-failure event damage was identified via an array of NDI techniques, which showed delaminations in the skin region between the notch tips and adjacent stringers. Teardown and visual inspection of the skin in the region from a notch tip to the adjacent stringer provided a ply-by-ply mapping of delamination and major crack and locations. SEM examinations of the fracture surfaces revealed that the fiber surfaces were clean of matrix material, which

indicated weak fiber/matrix interface and provided a plausible explanation for the widespread delaminations ahead of the notch tip. The fiber distribution and alignment was altered by the warp-knitting. Delaminated and disbonded surfaces showed matrix serrations, indicating shear (Mode II) failure. Examination of the failed stitches showed stitch stretching, tensile stitch failure mostly at the interface, and scattered stitch failure in the laminate with associated stitch pull-out.

Results from this test program apply directly to future progressive failure analysis of PRSEUS fuselage structure loaded in tension by: 1) showing that warp-knitting and stitching had an effect on the failure process and mechanisms and therefore must be considered and 2) providing experimental results for validation of the analytically predicted failure process.

ACKNOWLEDGEMENTS

The authors would like to acknowledge the participation and contributions of Mr. Kim Linton and Mr. Albert Neal of The Boeing Co. in the planning, design, pre-test analysis, and execution of the test and whose efforts were instrumental to the successful completion of the test program. The design of the modification of the FASTER facility for this test program was done by Mr. Gregory Korkosz, Boeing retired, who also played a key role the entire test program. The authors would like to express their deepest appreciation to Mr. Yongzhe Tian, Mr. Jeff Panco, and Mr. Patrick Sheehan of Hiasun, Inc. whose diligent efforts during the FASTER modifications and testing played an instrumental role in this team effort. The authors also wish to acknowledge Mr. Patrick Johnston of NASA Langley Research Center who performed numerous ultrasonic examinations of the panel. Acknowledgement is also due to Mr. Michael Bode, Mr. Michael Holle, Mr. Randy Duvall, Ms. Ciji Nelson, and Mr. Kyle Thompson at Sandia National Labs for planning and performing the posttest ultrasonic and CT inspections. Finally many thanks are due to the Drexel University Centralized Research Facility and Dr. Edward Basgall for making the SEM examinations possible.

REFERENCES

1. Dransfield, K. A., Baillie, C., and Mai, Y. W. 1994. “Improving the Delamination Resistance of CFRP by Stitching - A Review,” *Compos. Sci. Technol.* 50(3):305-317.
2. Mignery, L. A., Tan, T. M., and Sun, C. T. 1985. “The Use of Stitching to Suppress Delamination in Laminated Composites,” ASTM 876, pp.371-385.
3. Jain, L. K. 1994. “On the Effect of Stitching on Mode I Delamination Toughness of Laminated Composites,” *Compos. Sci. and Technol.*, 51(3):331-345.
4. Jain, L.K. and Mai, Y.-W. 1995. “Determination of Mode II Delamination Toughness of Stitched Laminated Composites,” *Comp. Sci. Technol.*, 55(3):241-253.
5. Cox, B. N. 1996. “Suppression of Delaminations in Curved Structures by Stitching,” *Compos. Part A Appl. Sci. Manuf.* 27(12):1133-1138.
6. Pelstring, R. M. and Madan, R. C. 1989. “Stitching to Improve Damage Tolerance of Composites,” presented at the 34th International SAMPE Symposium and Exhibition - Tomorrow's Materials: Today, May 8-11, 1989, Reno, NV.
7. Hawley, A. V. 1993. “Development of Stitched/RTM Primary Structures for Transport Aircraft,” NASA CR 191441.
8. Larsson, F. 1997. “Damage Tolerance of a Stitched Carbon/Epoxy Laminate,” *Compos. Part A: Appl. Sci. and Manuf.*, 28(11):923-924.

9. Dow, M. B., and Dexter, H. B. 1997. "Development of Stitched, Braided and Woven Composite Structures in the ACT Program and at Langley Research Center (1985-1997)," NASA/TP-97-206234.
10. Deaton, J. W., Kullerd, S. M., Madan, R. C., and Chen, V. L. 1992. "Test and Analysis Results for Composite Transport Fuselage and Wing Structures," presented at the 9th DOD/NASA/FAA Conference on Fibrous Composites in Structural Design, November 1991.
11. Jegley, D. C. 2007. "Improving Strength of Postbuckled Panels Through Stitching," *Compos. Struct.*, 80(2):298-306.
12. Tan, Y., Wu, G., Suh, S. S., Yang, J. M., and Hahn, H. T. 2008. "Damage Tolerance and Durability of Selectively Stitched Stiffened Composite Structures," *Int. J. Fatigue*, 30(3):483-492.
13. Velicki, A. and Thrash, P. J. 2008. "Advanced Structural Concept Development Using Stitched Composites," presented at the 49th AIAA/ASME/ASCE/AHS/ASC Structures, Structural Dynamics and Materials Conference, April 7-10, 2008, Chicago, IL.
14. Hoffman, K. May 2006. "Deliver Order 0059: Multi-role Bomber Structural Analysis," Air Vehicle Technology Integration Program (AVTIP) Final Report for 14 December 2004 – 08 May 2006, AFRL-VA-WP-TR-2006-3067.
15. Velicki, A., Yovanof, N., Baraja, J., Linton, K., Li, V., Hawley, A., Thrash, P., DeCoux, S. and Pickell, R. January 2011. "Damage Arresting Composites for Shaped Vehicles – Phase II Final Report," NASA CR-2011-216880.
16. Lovejoy, A. E., Rouse, M., Linton, K. and Li, V. P. 2011. "Pressure Testing of a Minimum Gauge PRSEUS Panel," presented at the 52nd AIAA/ASME/ASCE/SHS/ASC Structures, Dynamics, and Materials Conference, April 2011, Denver, CO.
17. Yovanof, N., Lovejoy, A. E., Baraja, J. and Gould, K. 2012. "Design, Analysis and Testing of a PRSEUS Pressure Cube to Investigate Assembly Joints," presented at the 2012 Airworthiness and Sustainment Conference, April 2-5, 2012, Baltimore, MD.
18. Li, V. P. and Velicki, A. 2008. "Advanced PRSEUS Structural Concept Design and Optimization," presented at the 12th AIAA/ISSMO Multidisciplinary Analysis and Optimization Conference, September 10-12, 2008, Chicago, IL.
19. Jegley, D. C. 2009. "Experimental Behavior of Fatigued Single Stiffener PRSEUS Specimens," NASA TM-2009-215955.
20. Velicki, A. September 2009. "Damage Arresting Composites for Shaped Vehicles, Phase I Final Report," NASA CR-2009-215932.
21. Jegley, D. C. 2010. "Influence of Impact Damage on Carbon-Epoxy Stiffener Crippling," presented at the American Society for Composites 25th Annual Technical Conference, September 20-22, 2010, Dayton, OH.
22. "Airworthiness Standards: Transport Category Airplanes," Title 14 Code of Federal Regulations, 2011.
23. Bakuckas, J. G., July 2002. "Full-Scale Testing of Fuselage Structure Containing Multiple Cracks," FAA report DOT/FAA/AR-01/46.
24. Linton, K. A., Neal, A., Mills, G., Velicki, A. and Thrash P. J. December 2010. "Design, Analysis, and Fabrication of a Curved PRSEUS Panel," Final Report for NASA contract NNL04AA11B/task order: NNL10AA99T.
25. Bergan, A. C., Bakuckas, J. G., Lovejoy, A. E., Jegley, D. C., Linton, K. A., Korkosz, G. J., Awerbuch, J. and Tan, T. M. 2011. "Full-Scale Test and Anaylsis of a PRSEUS Fuselage Panel to Assess Damage-Containment Features," presented at the 2011 Airworthiness and Sustainment Conference, April 18-21, 2011, San Diego, CA.
26. Bergan, A. C., Bakuckas, J. G., Lovejoy, A. E., Jegley, D. C., Linton, K. A., Neal, A., Korkosz, G. J., Awerbuch, J. and Tan, T. M. 2012. "Full-Scale Test and Analysis Results of a PRSEUS Fuselage Panel to Assess Damage-Containment Features," presented at the 2011 Airworthiness and Sustainment Conference, April 2-5, 2012, Baltimore, MD.
27. Khanolkar, A., Bergan, A. C., Ozevin, D. Bakuckas, J. G., Awerbuch J. and Tan, T.-M. 2012. "Monitoring Acoustic Emission in a PRSEUS Fuselage Panel under Combined Loading," presented at the American Society for Composites 27th Annual Technical Conference, October 1-3, 2012, Austin TX.
28. Mouritz, A. P., Bannister, M. K., Falzon, F. J., and Leong, K. H. 1999. "Review of Applications for Advanced Three-Dimensional Fibre Textile Composites," *Compos. Part A Appl. Sci. Manuf.*, 30(12):1445-1461.
29. Hayes, B. S. and Gammon, L. M. 2001. "Fractography" in *ASM Handbook, Volume 21: Composites*. D. B. Miracle and S. L. Donaldson, eds. ASM International, pp.977-987.